



## Open-section origami beams for energy absorption

Yang Li<sup>a,\*</sup>, Zhong You<sup>b</sup>

<sup>a</sup> Graduate Aerospace Laboratories, California Institute of Technology, 1200 E. California Blvd., Pasadena, CA, 91125, USA

<sup>b</sup> Department of Engineering Science, University of Oxford, Parks Road, Oxford, OX1 3PJ, UK



### ARTICLE INFO

#### Keywords:

Energy absorption  
Origami  
Beams  
the Brazier's effect

### ABSTRACT

A series of novel open-section beams employing origami geometries were developed. These beams overcame the Brazier's effect, and they can provide more constant bending resistance and overall higher energy absorption than conventional open-section beams. Numerical simulations and experiments were used to validate these designs and showed that properly designed origami beams can achieve 23.0–40.0% higher energy absorption and 12.7–20.7% lower load uniformity than conventional beams under quasi-static loading.

### 1. Introduction

The frames of vehicles, which consist primarily of thin-walled structures, are used to protect passengers during accidents, as shown in Fig. 1(a). They are designed to absorb kinetic energy through large plastic deformations when subjected to impact loadings. Thin-walled tubes under axial compression and thin-walled beams under lateral bending are commonly used. Steel and aluminium alloy are commonly used to construct these tubes and beams due to their high machinability and low cost. There are two favourable energy absorption properties that should be taken into account when designing these tubes and beams. One is high specific energy absorption (SEA), which is defined as the energy absorbed per unit mass, and the other is low load uniformity (LU), which is defined as the ratio between the peak load and the mean crush load [1]. Thin-walled beams have a relatively low SEA compared to tubes under axial compression. This result is due to the large span-to-depth ratio and the bending deformation mode of the beam, which leads to relatively little strain when crushed laterally. Another problem is that thin-walled beams exhibit the Brazier's effect [2] associated with the bending deformation mode, i.e., transverse webs that connect the top and bottom flanges are under compression during large bending deformations, leading to a reduction in the cross-sectional height, as shown in Fig. 1(b). This effect causes a significant and monotonic decrease in the bending resistance in the later stage of deformation [3], and it results in low SEA and high LU.

Attempts were made to alter the bending deformation mode of conventional beams into tension or compression modes to avoid these problems. By introducing tension components at the back of a curved beam, a membrane deformation mode can be triggered [4]. Although it has

higher energy absorption, this type of beam is also heavier and does not integrate well with the main structure of a vehicle. Similarly, improvements in the energy absorption of curved beams can be achieved by altering the bending mode to a compression mode under specific loading and boundary conditions [5]. To improve the performance of the bending mode itself, additional short transverse stiffeners can be added to the webs of the beam to resist the reduction of cross-sectional height during a large deformation, potentially alleviating the Brazier's effect [6]. Efforts have also been made to use different materials to increase the energy absorption of beams [7]. However, little has been done to eliminate the Brazier's effect present in the bending deformation mode completely.

Eliminating the Brazier's effect, i.e., maintaining the cross-sectional height of the beam during large deformations, might produce a sustainably high bending resistance, which does not reduce significantly and monotonically. In this paper, new designs for thin-walled, open-section beams are proposed which can overcome the section height reduction problem associated with existing beams. Contrary to the compression experienced by the transverse webs in the Brazier's effect, tension is dominant in most of the webs in these new designs. All these new beams can be created by folding (stamping) a thin-walled sheet material according to particular origami patterns, making manufacturing them easy. The design of these origami beams is provided in Section 2. Small-scale experiments and corresponding simulations are carried out in Section 3. Then extensive numerical simulations of a conventional beam and origami beams are conducted in Section 4. The further development of origami beams into panels, curved beams, and curved panels is proposed and examined preliminarily in Section 5. Section 6 contains the conclusions and directions for future research.

\* Corresponding author.

E-mail address: [chineseguyliyang@gmail.com](mailto:chineseguyliyang@gmail.com) (Y. Li).

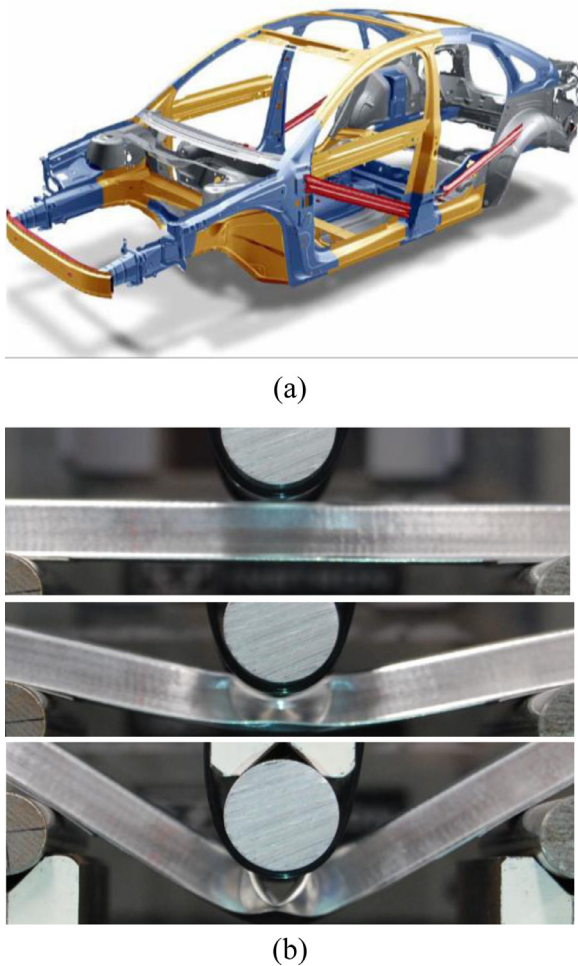


**Fig. 1.** (a) The frame of a vehicle and (b) the Brazier's effect on bending a thin-walled beam.

## 2. Geometry of origami beams

The essential idea behind this improvement in geometry is to: (1) replace the uniform cross-sectional beam with several longitudinally-repetitive modules for a more sustainable bending resistance during large deformations; and (2) create the modules in such a way that they have the ability to maintain their section heights during large bending deformations. The geometric solution which satisfies these two criteria follows.

The origami pattern shown in Fig. 2(a) consists of a set of mountain and valley creases, represented by solid and dashed lines, respectively. It is a rigid origami pattern, i.e., continuous folding can be carried out by folding along the creases without stretching the sheet, as Fig. 2(b) shows. A straight beam can be formed once faces A and B are meet and are welded together, as shown in Fig. 3(a). In Fig. 3(a), the surface facing up is called the *top face*, and is designed to take compression, and the surface facing down, which is designed to resist tension, consists of the *bottom webs*.

The geometry of this beam is defined by seven independent parameters, where  $\alpha$  is the pattern angle;  $a$ ,  $b$ ,  $c$  and  $d$  are the dimensions, all of which are given in Fig. 2(a); and  $m_b$  and  $n_b$  are the numbers of units (one of the units is pointed out in Fig. 3(a) and (b)) along the lateral and longitudinal directions of the beam, respectively. For example, the beam in Fig. 3(a) has 4 lateral units ( $m_b = 4$ ), while the pattern and beam in Fig. 2 each has 2 lateral units ( $m_b = 2$ ). A portion of a completed beam with 2 lateral units ( $m_b = 2$ ) folded from an aluminium sheet is shown in Fig. 3(c).

Geometrically, it can be found that the angle between the top surface and horizontal plane, shown in Fig. 3(a) and (b), is

$$\theta = \arcsin(\tan \alpha) \quad (1)$$

Other geometric parameters shown in Fig. 2(a) are

$$g = 2a \sin \alpha \quad (2)$$

and

$$b_1 = b - g \quad (3)$$

The overall length of the beam is

$$L = n_b(2a \cos \alpha \cos \theta + c) \quad (4)$$

while the width of the beam is

$$W = m_b b \quad (5)$$

The overall height, shown in Fig. 3(a) and (b), is

$$h_b = d + a \cos \alpha \cos \theta, \quad (6)$$

and the surface area of the beam is

$$A_1 = n_b \left( 2a \cos \frac{\alpha}{2} + c \right) [m_b(b + 2d) + 2d] \quad (7)$$

Repetitive units can be observed from in the geometry of this origami beam, and this feature aims at distributing the deformation over multiple units for a more sustainable bending resistance. The top face of the beam is designed as the compression side, and has a zigzag shape, as shown in Fig. 3(b). Since the valleys of the zigzag shape at two sides (the grey area) are welded together, the top face of the beam can only be squeezed up instead of being crushed down, as demonstrated in Fig. 4. This effect generates tension vertically in the webs (in the middle), and this will maintain the section height of the beam for a sustainably large reaction response, contrary to the compression observed in the Brazier's effect on traditional beams. Experimental and numerical analysis were carried out for the validation of this design, with the results provided in the next section.

## 3. Experimental study and its comparison with the numerical results

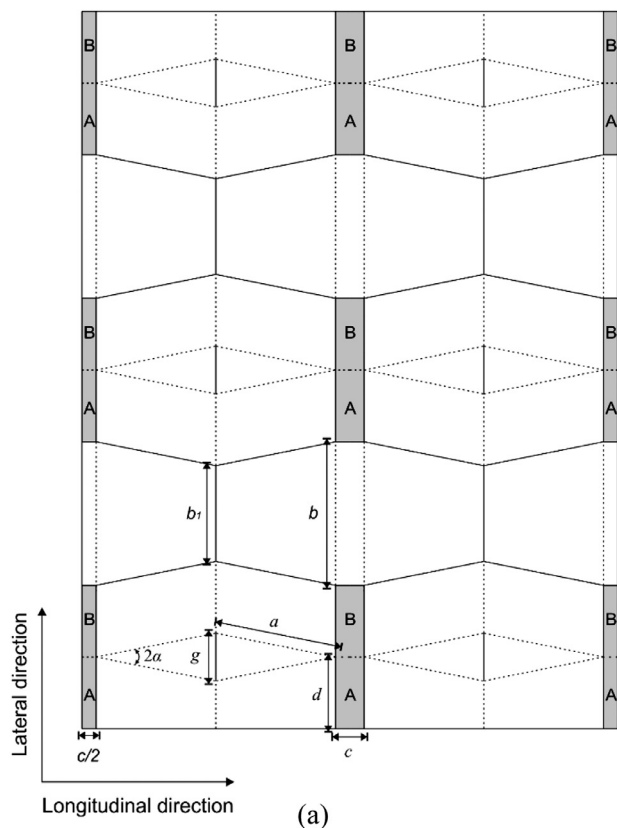
This section is meant to demonstrate the function of the origami beam and its merits compared to a conventional beam with experiments, while also serving to validate the numerical modelling technique.

The origami beam is designed for absorbing impact energy, and can be used widely in automobile frames, guardrails, mining structures, and so forth. Specifically, in this paper, the effectiveness of the origami beam is evaluated by comparing it with a commercial bumper beam, as shown in Fig. 5(a). The cross-section of this bumper beam (note that it has been simplified as a straight beam) is shown in Fig. 5(b). SEA and LU are used to evaluate their energy absorbing performances, and quasi-static loading was employed.

### 3.1. Experimental setting

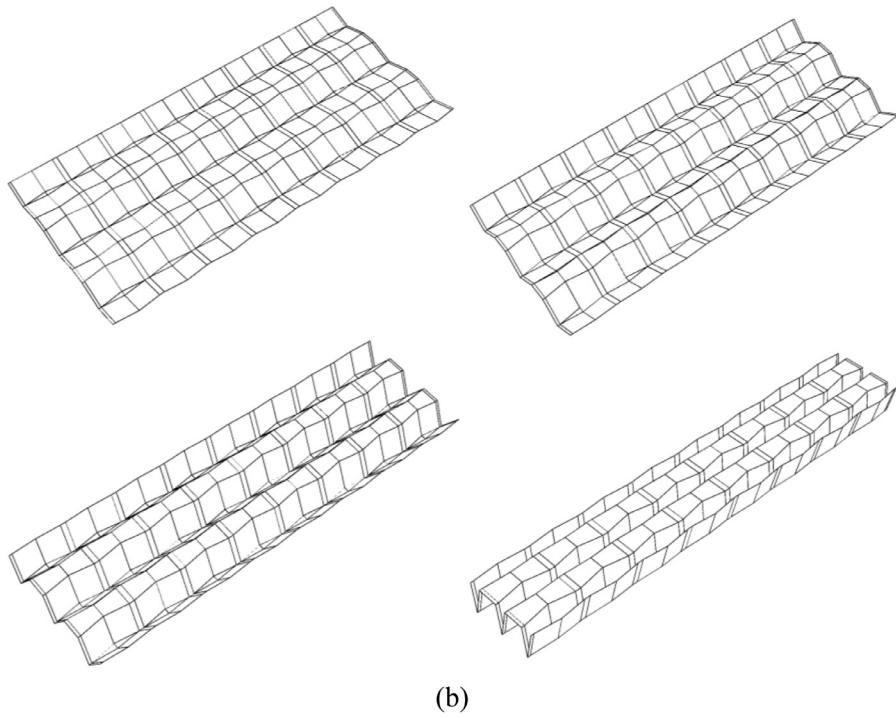
Small-scale prototypes  $B_{0,\text{exp}}$  and  $B_{1,1,\text{exp}}$  used the same amount of material and have the same length (200 mm) and depth (11 mm).  $B_{0,\text{exp}}$  and  $B_{1,1,\text{exp}}$  are scaled-down version of  $B_0$  and  $B_{1,1}$ , whose geometric parameters are given in Table 1. The scale-down ratio used was 1/5, with the exception of a 1/10 ratio for thickness. The scale ratio for the thickness was different due to material availability, and manufacturing and loading feasibility.

All beams were constructed from 0.2 mm-thick aluminium 1100-O. Tensile tests were conducted on the material, resulting in the



(a)

**Fig. 2.** The design of origami beams: (a) a portion of the origami folding pattern on a sheet material, where solid and dashed lines represent mountain and valley creases, respectively; (b) a gradual folding schematic diagram.



(b)

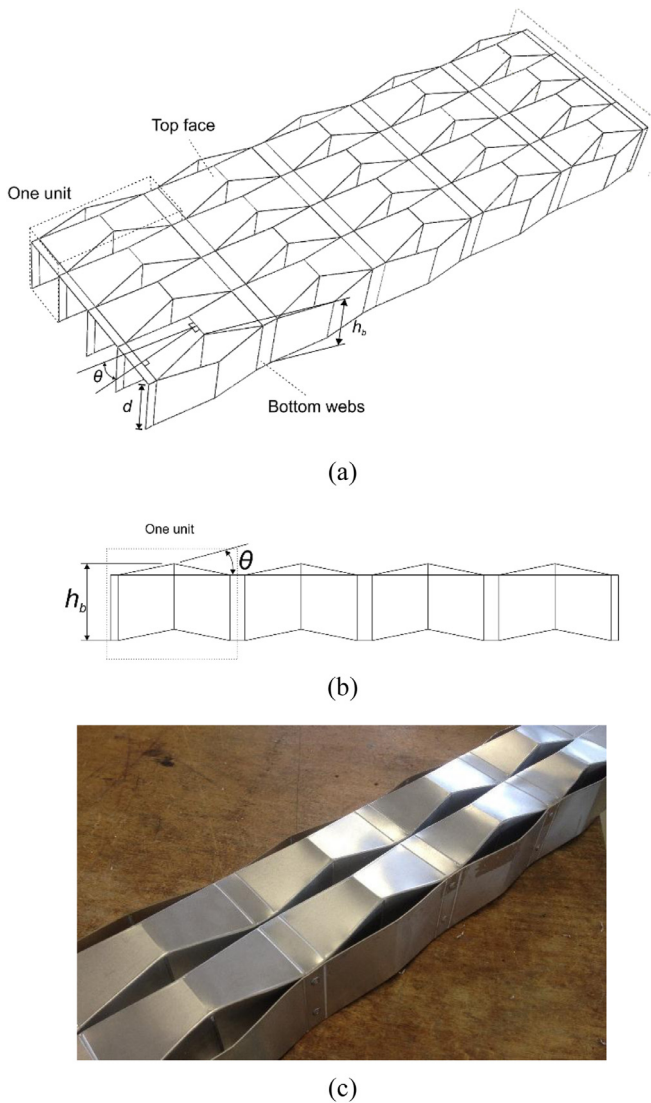


**Fig. 3.** Folded geometry: (a) the beam obtained from folding the sheet, with grey parts in Fig. 2(a) bonded together; (b) side view of the design; and (c) an aluminium model.

stress-strain curve shown in Fig. 6. The beams were built by gradually stamping the sheet material with 3D-printed male and female molds, as shown in Fig. 7. A similar stamping technique was used in [8,9]. This process provides a simple way to fold and form the beams into shape. The material had good ductility, and the residual stress from the manu-

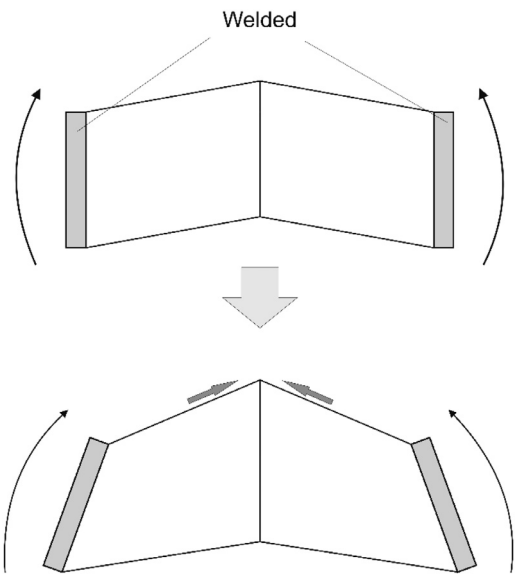


**Fig. 4.** Schematic diagram of the side view of one unit under pure bending.

facturing process was very small comparing to the stress experienced in the crushing process. Parts which need to be welded in full-size origami beams were glued with superglue (cyanoacrylate). The two ends of the beams were made sufficiently rigid by wrapping them with glued-on additional material, as noted in Fig. 7(b). Beams were put under an Instron 5582 for three-point bending tests, as shown in Fig. 8. The span between supports was 100 mm, the rigid rod at centre had a radius of 10 mm, and support rods had radii of 7.5 mm. The loading speed was 5 mm/min, and total displacement was 40 mm. In total, three specimens were prepared for each type of beam, and all of them are presented in Fig. 7(b).

### 3.2. Numerical modelling of beams

Numerical models of  $B_{0,\text{exp}}$  and  $B_{1,1,\text{exp}}$  are shown in Fig. 9. The two ends were stiffened with more material as in the experiments. Here, 19088 S4R elements were used for  $B_{0,\text{exp}}$ , and 22960 S4R and 32 S3 elements were used for  $B_{1,1,\text{exp}}$ . The settings for the loading and supports were the same as in the experiment. The loading speed was 1 m/s (different from the experiment), and the kinematic energy was well below 5% of the total energy, allowing it to be considered quasi-static. Convergence tests with respect to mesh density and analysis time were conducted prior to the analysis. The ratio of artificial energy to internal energy was below 5% as recommended by Abaqus/Explicit [10].

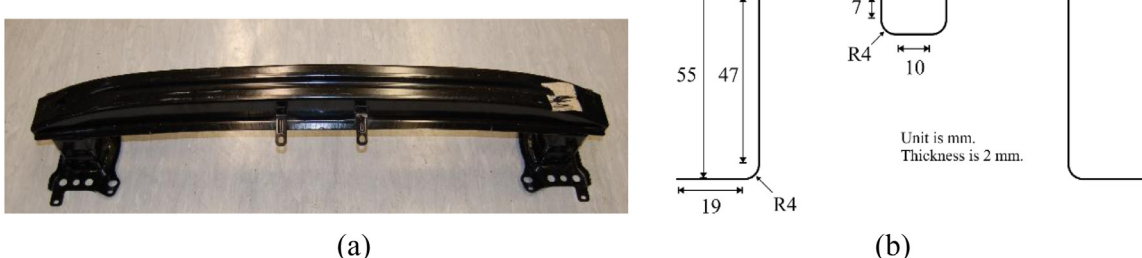


**Fig. 5.** (a) A commercial bumper beam and (b) its cross-section.

**Table 1**  
Information for all simulated beams.

Model	$n_b$	$\alpha$ (°)	b (mm)	Weight (kg)	Unstable failure	LU	LU reduction (%)	SEA (J/kg)	SEA increase (%)
B <sub>0</sub>	—	—	—	4.15	—	1.5	—	639.5	—
B <sub>1,1</sub>	10	6.3	35	4.12	—	1.28	14.7	786.6	23.0
B <sub>1,2</sub>	10	6.3	30	4.04	—	1.31	12.7	815.5	27.5
B <sub>1,3</sub>	10	6.3	25	3.96	—	1.24	17.3	852.5	33.3
B <sub>1,4</sub>	10	6.3	20	3.88	—	1.19	20.7	856.3	33.9
B <sub>1,5</sub>	10	6.3	15	3.80	Unstable	1.37	8.67	494.3	-22.7
B <sub>1,6</sub>	12	6.3	25	3.96	—	1.19	20.7	831.7	30.1
B <sub>1,7</sub>	12	6.3	20	3.88	—	1.24	17.3	874.5	36.7
B <sub>1,8</sub>	14	6.3	25	3.96	Unstable	1.20	20.0	617.2	-3.49
B <sub>1,9</sub>	14	6.3	20	3.87	Unstable	1.25	16.7	578.4	-9.55
B <sub>2,1</sub>	10	3.8	35	4.10	—	1.19	20.7	801.3	25.3
B <sub>2,2</sub>	10	3.8	30	4.02	—	1.24	17.3	819.4	28.1
B <sub>2,3</sub>	10	3.8	25	3.94	—	1.21	19.3	854.5	33.6
B <sub>2,4</sub>	10	3.8	20	3.86	—	1.20	20.0	871.4	36.3
B <sub>2,5</sub>	10	3.8	15	3.78	Unstable	1.42	5.33	485.1	-24.1
B <sub>2,6</sub>	12	3.8	25	3.94	Unstable	1.17	22.0	631.1	-1.31
B <sub>2,7</sub>	12	3.8	20	3.86	—	1.20	20.0	895.5	40.0
B <sub>2,8</sub>	14	3.8	25	3.94	Unstable	1.27	15.3	607.6	-4.99
B <sub>2,9</sub>	14	3.8	20	3.86	Unstable	1.06	29.3	706.3	10.4
B <sub>3,1</sub>	10	1.6	30	4.02	Unstable	1.20	20.0	686.6	7.36
B <sub>3,2</sub>	10	1.6	20	3.86	Unstable	1.17	22.0	696.9	8.98

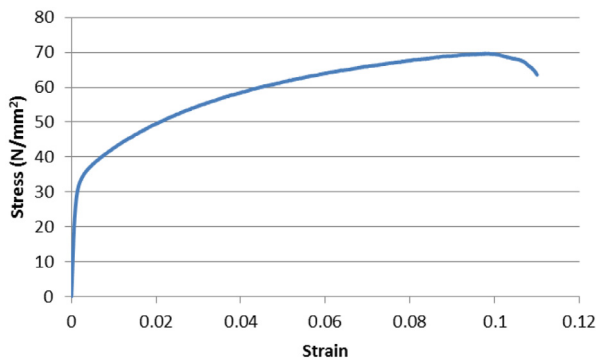


Fig. 6. Stress-strain curve of aluminium 1100-0.

### 3.3. Experimental and numerical results

Six experiments and two simulations were conducted as described in the previous subsections. One set of experimental and simulated deformations of B<sub>0,exp</sub> are presented in Fig. 10 for respective displacements of 0 mm, 20 mm, and 40 mm. In total, three experiments for B<sub>0,exp</sub> were carried out and showed similar deformations. Reaction curves for the three experiments are given in Fig. 13(a), and good consistency can be seen. There are no obvious discrepancies between the experimental and simulated deformations in Fig. 10. The average reaction curve

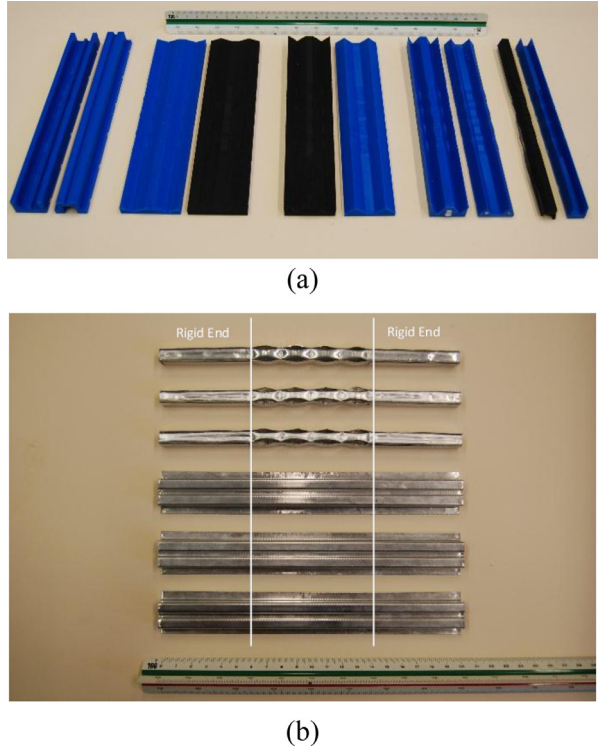


Fig. 7. Manufacturing via (a) a series of moulds and (b) forming 6 beam prototypes.

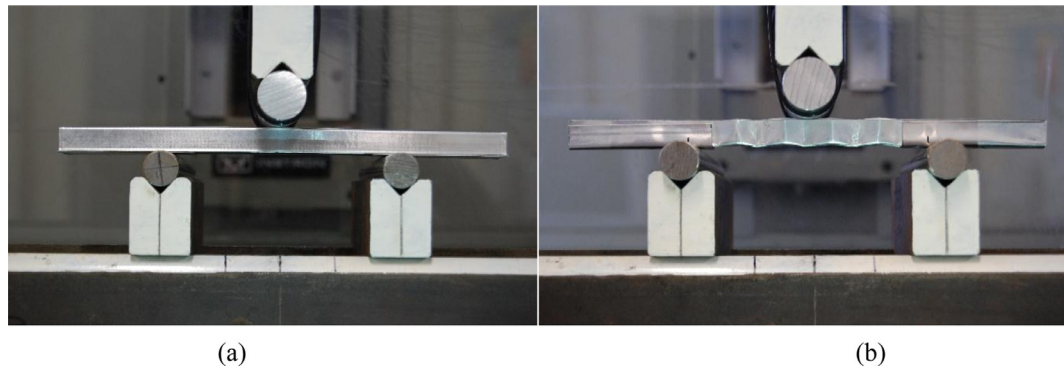
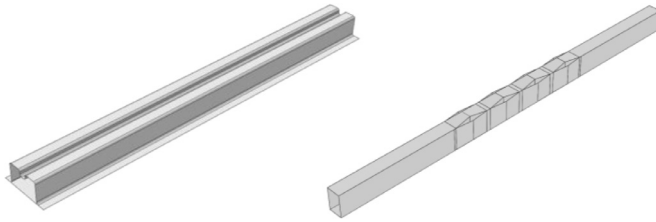


Fig. 8. The setting for the three-point bending of (a) B<sub>0,exp</sub> and (b) B<sub>1,1,exp</sub> in the Instron.



**Fig. 9.** Geometries of the numerical models of  $B_{0,\text{exp}}$  and  $B_{1,1,\text{exp}}$ .

for the experiments and the reaction curve for the numerical simulation are shown in Fig. 14(a) and provide a generally good match between the two, except for a slight fluctuation in the numerical simulation. This fluctuation was probably due to some numerical noise, a slight dynamic bouncing effect, and frictional sliding at the supports (the penalty method was employed in simulations). A significant section height reduction could be observed for  $B_{0,\text{exp}}$  in both the experiment and simulation. This reduction corresponds to the huge decrease of stiffness in the later stage of deformation, as shown in Fig. 13(a) and 14(a).

One set of experimental deformations of origami beam  $B_{1,1,\text{exp}}$  is shown in Fig. 11. The cross-section in the middle of the beam is increasing instead of reducing, as intended (illustrated in Fig. 4), which indicates the elimination of the Brazier's effect. Its comparison with the numerical deformations is presented in Fig. 12. In comparison with  $B_{0,\text{exp}}$ , the top face of  $B_{1,1,\text{exp}}$  bulged out instead of being crushed down in both the experiment and simulation. In total, three experiments were done and exhibited similar failure modes. The experimental reactions of  $B_{1,1,\text{exp}}$  are shown in Fig. 13(b). They show some phase shifting and magnitude variations, mainly due to their highly imperfect manufacturing process. The performances of  $B_{1,1,\text{exp}}$  still demonstrated good repeatability in terms of deformation and the reaction curves, suggesting that the manufacturing method was acceptable and the design is not sensitive to imperfections. The average reaction curve from the experiments and the reaction curve from the numerical simulation involving  $B_{1,1,\text{exp}}$  are shown in Fig. 14(b), and the numerical simulation gave an overall higher reaction than the average for the experiments. The initial peak force of the origami beam was lower in the experiments than it was in the simulation, a result most likely due to its highly imperfect initial geometry, which was not considered in the simulation. The lower overall reaction forces in the experiments compared to the simulation could be caused by the lack of consideration of the strength of the su-

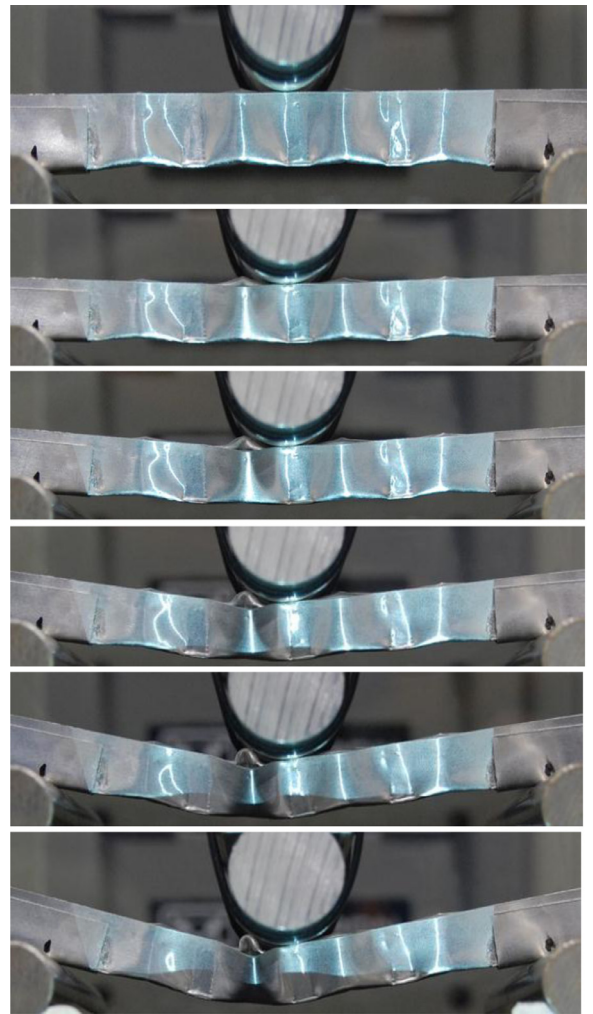


**Fig. 11.** Experimental deformation of an origami beam.

perglue in the numerical analysis since the superglue could be heard splitting in the later stage of loading during the experiments. Again, the fluctuations in numerically simulated reactions could be caused by numerical noise, the dynamic bouncing effect (affecting only the reaction

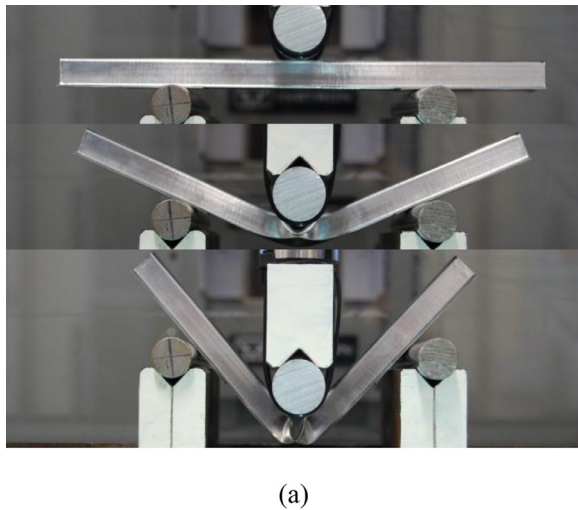


**Fig. 10.** (a) Experimental and (b) numerical deformation of  $B_{0,\text{exp}}$ .

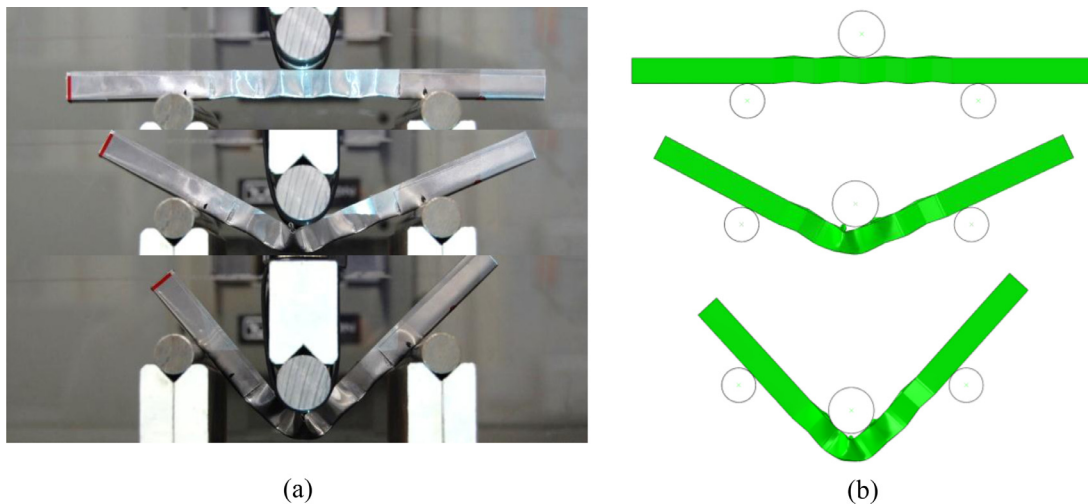


Fig. 12. (a) Experimental and (b) numerical deformations of  $B_{1,1,\text{exp}}$ .

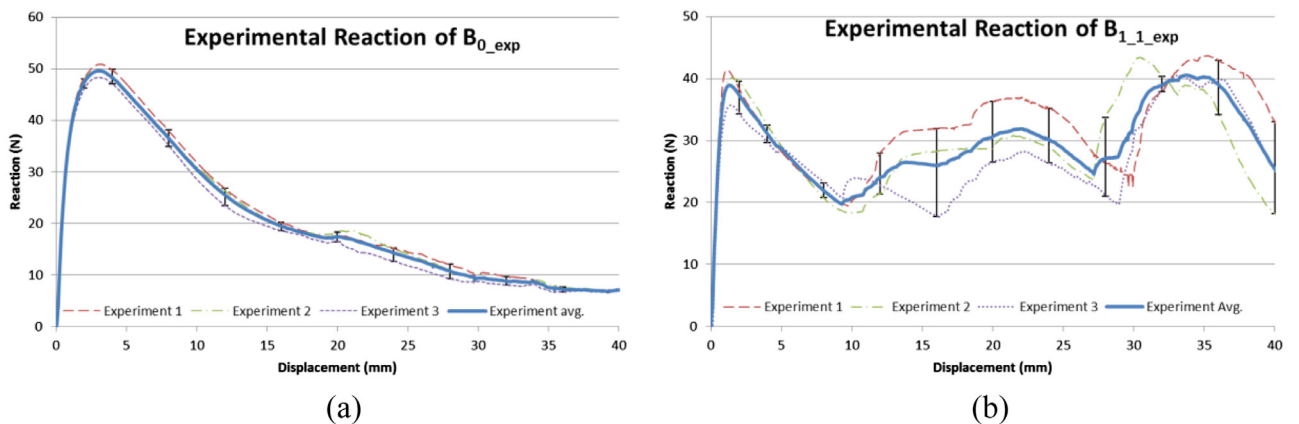


Fig. 13. Experimental reactions of (a)  $B_{0,\text{exp}}$  and (b)  $B_{1,1,\text{exp}}$ .

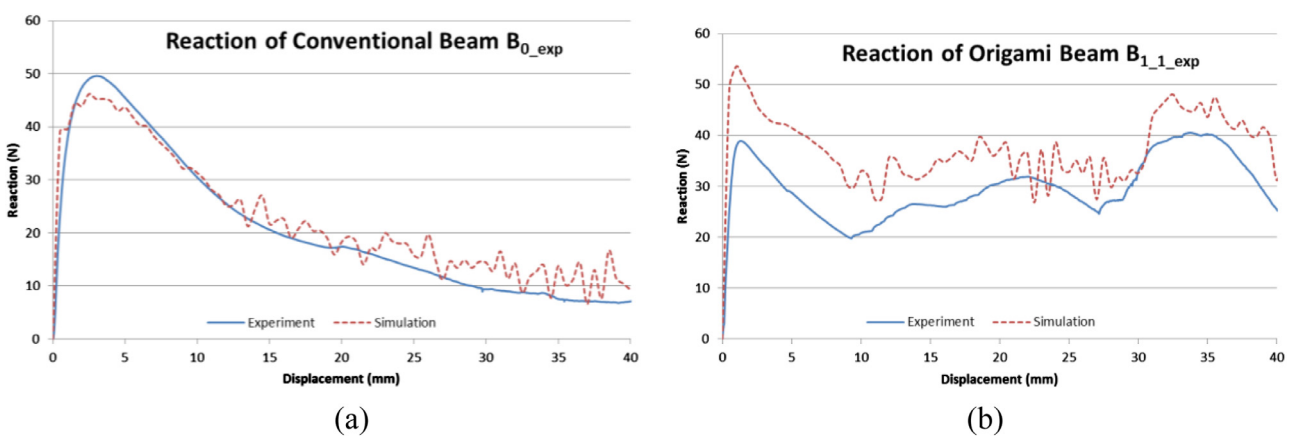


Fig. 14. Comparison between experiments and numerical simulations of (a)  $B_{0,\text{exp}}$  and (b)  $B_{1,1,\text{exp}}$ .

**Table 2**  
Results of experimental and numerical analysis.

Types	Mean crush force (N)		Load uniformity		Increase of mean crush force		Decrease of load uniformity	
	Exp.	FEA	Exp.	FEA	Exp.	FEA	Exp.	FEA
B <sub>0</sub> _exp	20.65	22.38	2.40	2.07	–	–	–	–
B <sub>1_1</sub> exp	29.61	37.31	1.37	1.44	43.40%	66.71%	42.98%	30.41%

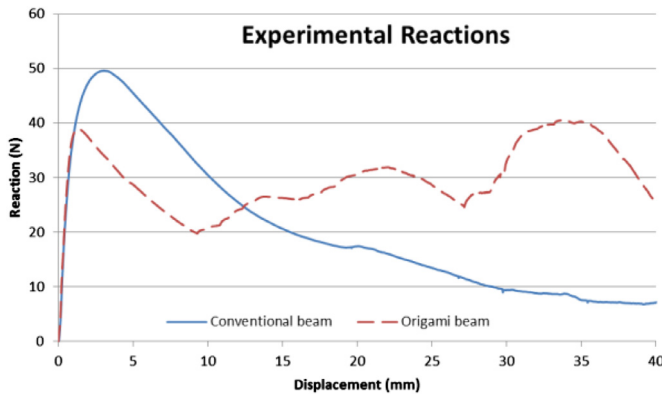


Fig. 15. Comparison of experimental reactions of B<sub>0</sub>\_exp and B<sub>1\_1</sub>exp.

force but not so much of the total energy in the end), and sliding at the supports.

A direct comparison of the experimental reactions of the conventional beam and the origami beam is shown in Fig. 15, highlighting that the origami beam B<sub>1\_1</sub>exp had a more constant reaction and an overall significantly higher energy absorption. The improvements exhibited by the origami beam B<sub>1\_1</sub>exp over the conventional beam B<sub>0</sub>exp are shown in Table 2. Specifically, there is a 40–60% increase in SEA and 30–40% decrease in LU in the origami beam compared to the conventional beam.

In this section, the improved performance of the origami beam compared to that of the conventional beam was experimentally confirmed. This proves directly that this new design can enable beams to eliminate the Brazier's effect during bending deformation and provide more consistent bending resistance in large deformations. The numerical simulation technique used was validated via its good correlation to experimental results.

#### 4. Parametric study of origami beams through numerical simulations

In this section, a series of numerical simulations were run to demonstrate that properly designed origami beams have significantly higher SEA and lower LU than a typical conventional beam.

Commercial bumper beam B<sub>0</sub>'s cross-section is shown in Fig. 5(b). Note that it has a material thickness of 2 mm and length of 1000 mm. A series of origami beams, 20 in total, were constructed in Abaqus with identical material thicknesses, spans, and cross-sectional heights to those of B<sub>0</sub>. The amount of material used for each origami beam was less than that used for the conventional beam B<sub>0</sub>. All origami beam models and their corresponding parameters are listed in Table 1. In addition, each origami beam model met the specifications  $m_b = 1$ ,  $t = 2$  mm,  $c = 10$  mm,  $d = 55$  mm, and  $L = 1000$  mm. The geometries of B<sub>0</sub> and B<sub>1\_1</sub> are shown in Fig. 16. All beams were subjected to quasi-static three-point bending, which was created by having one rigid cylinder press down in the middle of the beam while the two ends of the beam were simply supported. The rigid cylinder had a radius of 50 mm, crushing speed of 5 m/s, and total displacement of 350 mm.

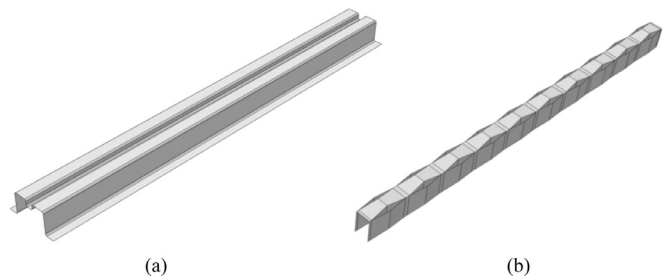


Fig. 16. The geometry of (a) B<sub>0</sub> and (b) B<sub>1\_1</sub>.

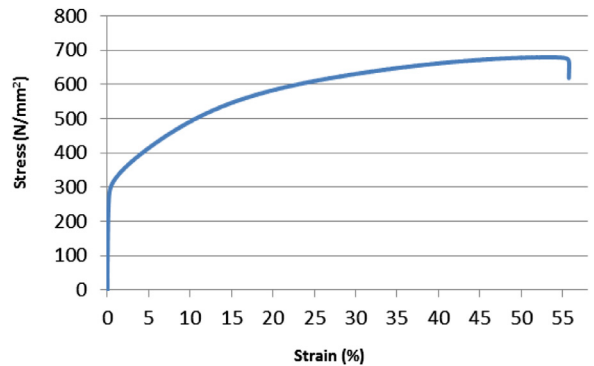
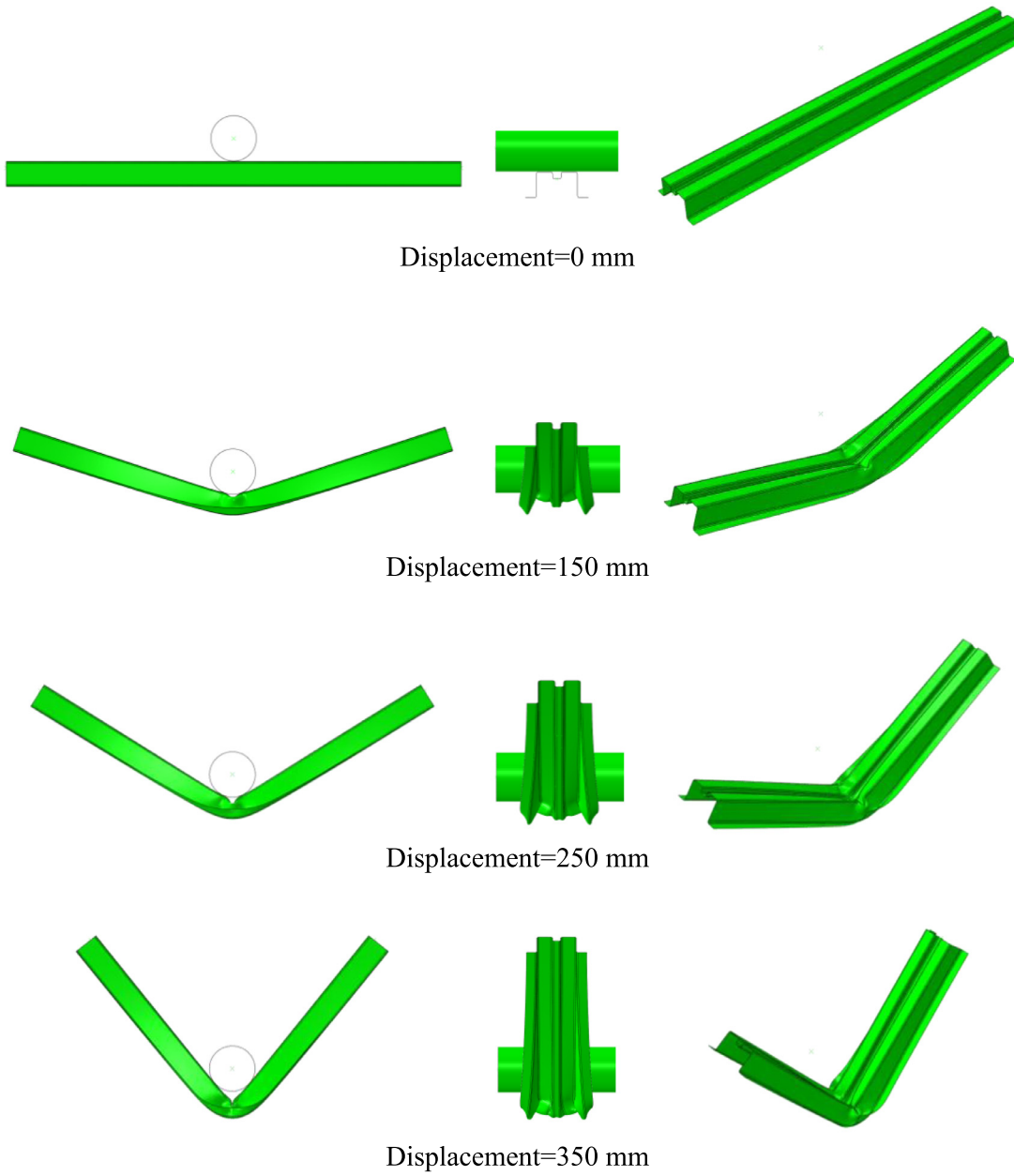


Fig. 17. Stress-strain curve of 304 stainless steel.

The beams were constructed of 304 stainless steel, which has the stress-strain curve shown in Fig. 17. Its material properties, which were obtained through dog-bone tests and the data sheet, are as follows: density  $\rho = 8030$  kg/m<sup>3</sup>, Young's Modulus  $E = 193$  GPa, Poisson's ratio  $\nu = 0.3$ , yield stress  $\sigma_y = 241.3$  MPa, ultimate stress and strain  $\sigma_u = 679.6$  MPa,  $\epsilon_u = 55.8\%$ , and frictional coefficient  $\mu = 0.25$  [5,8,9,11]. Abaqus/Explicit [10] was used to simulate the performance of the beams under quasi-static three-point bending.

The numerical results for all 21 beam models are presented in Table 1, which contains information on the failure mechanism for the origami beams, as well as their comparisons with the conventional beam in terms of SEA and LU. The deformation of B<sub>0</sub> provided by the numerical simulation is shown in Fig. 18, illustrating the deformation of the beam from three different angles: side view, front view, and inclined view (the rigid rod was removed). The material in the middle of the beam was squeezed downwards, and a localised hinge was formed. In consequence, an obvious section-height reduction occurred in the middle of the beam (the Brazier's effect), which caused a significant decrease of stiffness in the later stage of bending.

The deformation of the origami beam B<sub>1\_1</sub> is shown in Fig. 19. Two units on the top face were squeezed up, and the section height was increased in this region. This behaviour implies that the bending resistance of the beam was better maintained than the conventional beam in a large deformation. Using the appropriate parameters, webs of origami beams could be widened during deformation to prevent lateral buckling, as shown in the front view of Fig. 19. All other stably deformed origami

Fig. 18. Deformation of  $B_0$ .

beams showed deformations similar to that of  $B_{1,1}$ . The reaction curves of  $B_0$  and  $B_{1,1}$  are presented in Fig. 20, highlighting that  $B_{1,1}$  achieved a more constant reaction than  $B_0$ . The fluctuation in reactions at the beginning was caused by a slight dynamic bouncing effect from the rigid cylinder hitting the beam initially. Table 1 shows that unstable failures of origami beams can occur when the width of the web or beam is too small and leads to low energy absorption. The deformation of  $B_{3,1}$  is shown in Fig. 21. Here, the material in top face bulged out at first, while webs of the beam swayed laterally when bent further, causing the reduction in bending resistance in the later stage. All other origami beams listed in Table 1 which failed unstably deformed in a similar way and caused relatively low energy absorption. As seen in Table 1, appropriately designed origami beams (excluding those which failed unstably) achieved 23.0–40.0% higher SEAs and 12.7–20.7% lower LUs than the conventional open-section beam  $B_0$ .

This unstable failure of origami beams (see Fig. 21), is essentially caused by the lateral torsional buckling. A smaller value of  $b$ , i.e., the

**Table 3**  
Appropriate ranges of parameters.

Parameters	$n$	$\alpha$ (°)	$b$ (mm)
Range	10	3.8–6.3	25–35

width of the one unit, and a large value of  $\alpha$ , which is associated with the width of the web and compression resistance of the top surface, can increase the SEA of origami beams. However, they also decrease the lateral rigidity of the beam and webs, resulting in the reduction of the stability of the structure. The effects of  $b$  and  $\alpha$  are shown in Fig. 22(a). This issue can be resolved by introducing more lateral units ( $m_b > 2$ ). Increasing  $n$  also decreases the stability, as shown in Fig. 22(b). In order to avoid an unstable failure, appropriate ranges of parameters for origami beams are proposed in Table 3, with the predetermination  $m_b = 1$ ,  $t = 2$  mm,  $c = 10$  mm,  $d = 55$  mm, and  $L = 1000$  mm. Scalability has been investi-

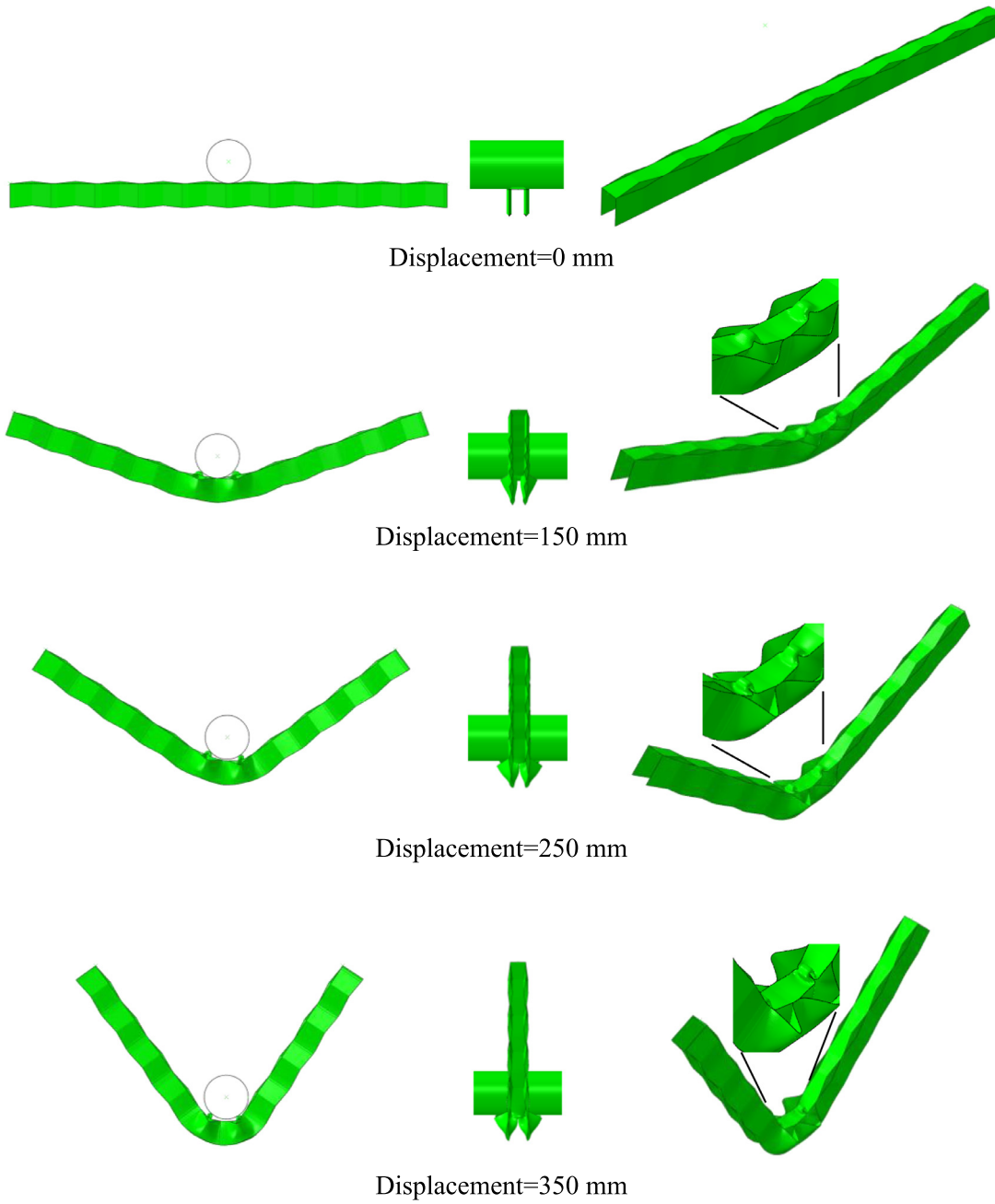


**Fig. 19.** Deformation of  $B_{1,1}$ .

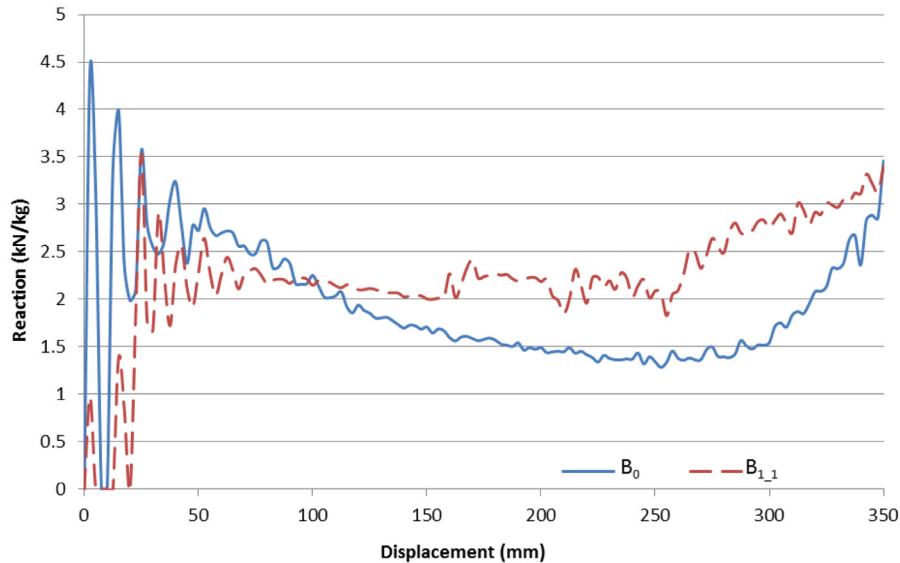
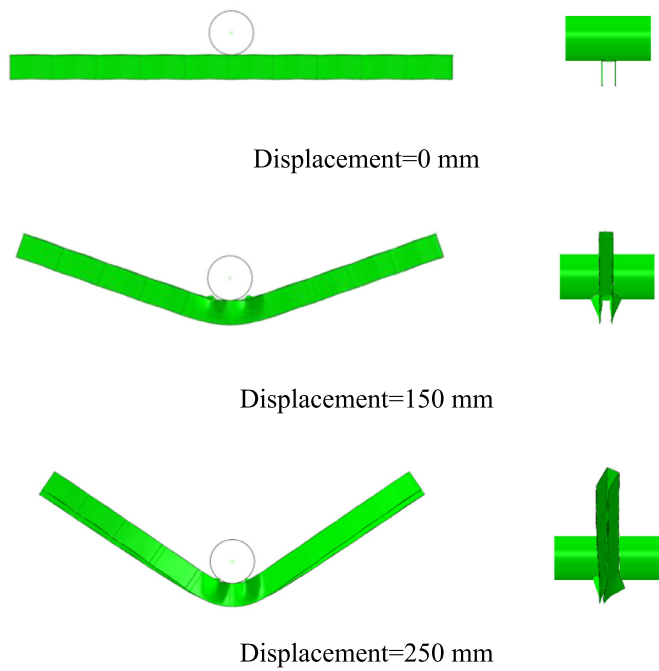
gated, and these parameter ranges can be used at different scales. Within the table, the beam  $B_{1,3}$  with  $\alpha = 6.3^\circ$  and  $b = 25 \text{ mm}$  is most optimized, while the beam  $B_{1,1}$  with  $\alpha = 6.3^\circ$  and  $b = 35 \text{ mm}$  is most conservative. Simulation results for origami beams at different settings and scales can be found in [12].

## 5. Preliminary development based on origami beams

As the previous sections demonstrated, the origami beams have a desired failure mechanism which enables high SEA and low LU. A similar failure mechanism can be also triggered in other forms of origami beams, panels, and curved beams. Related designs are presented and discussed in this section.

### 5.1. Origami panels

Panels can be made when origami beam are repeated laterally. If the  $m_b$  of  $B_{1,3}$  is set to 2, then 4, the new beams or panels can be named  $B_{1,3,2}$  and  $B_{1,3,4}$ , respectively, as shown in Fig. 23(a). These structures can be manufactured from a single sheet of material according to the folding pattern shown in Fig. 2(a) by employing more repetitions in the lateral direction of the origami pattern. The corresponding numerically simulated deformations are shown in Fig. 22(b). The SEAs of  $B_{1,3}$ ,  $B_{1,3,2}$ , and  $B_{1,3,4}$  were 852.5, 981.9, and 1120.5 J/kg, respectively. It was observed generally that a larger  $m_b$  contributes to a significantly larger SEA. This is because the material at the two lateral sides of the beam/panel absorbs less energy than the material in the middle, and the larger  $m_b$  reduces the proportion of material at the sides, which increases the SEA.

Fig. 20. Reactions of  $B_0$  and  $B_{1,1}$ .Fig. 21. Side and frontal view of deformation of  $B_{3,1}$ .

Larger values of  $m_b$  also increase the stability of the beam/panel due to the increase in its overall width, perhaps enabling further optimization. Increasing  $m_b$  can extend origami beams into panels, which might suit different applications.

### 5.2. Face-switcher

The top face of the beam is designed to resist compression, and the bottom webs are used to take tension. However, there are situations in which the bending moment switches its sign within the beam, such as in continuous beams with supports in the middle or with clamped boundary conditions. For instance, the standard boundary condition of bumper beams is ‘clamped at two ends’ [13]. As a consequence, the geometry of the origami beam needs to be switched upside down correspondingly within the beam, which leads to a special design called *face-switcher*.

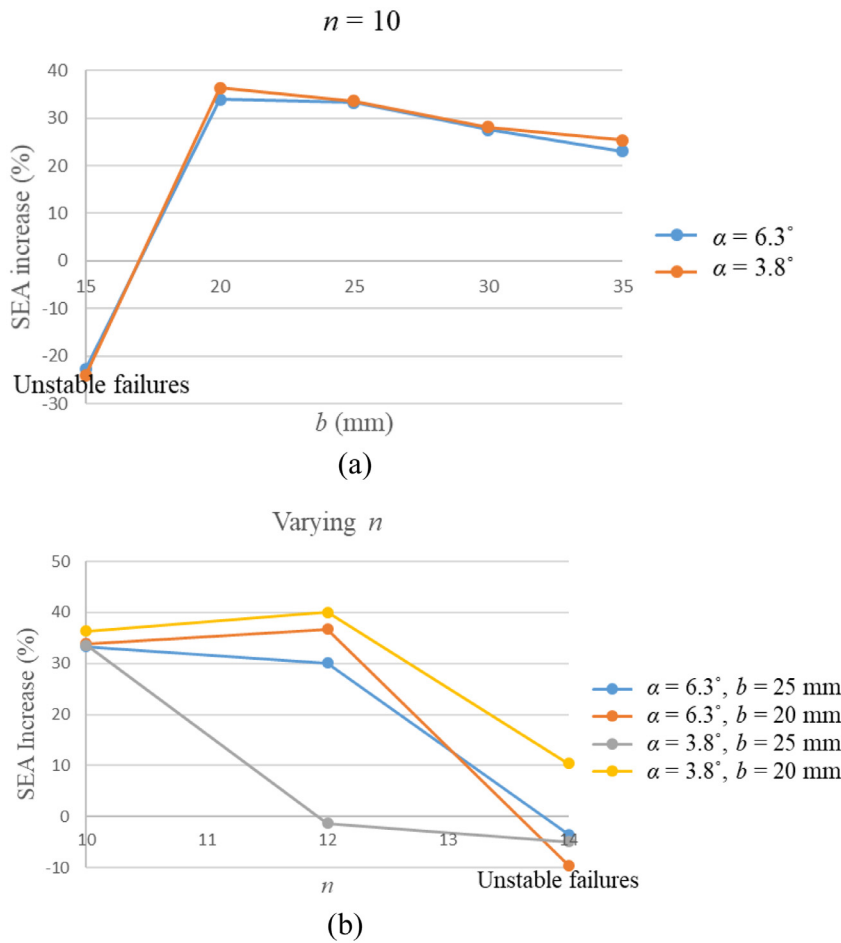
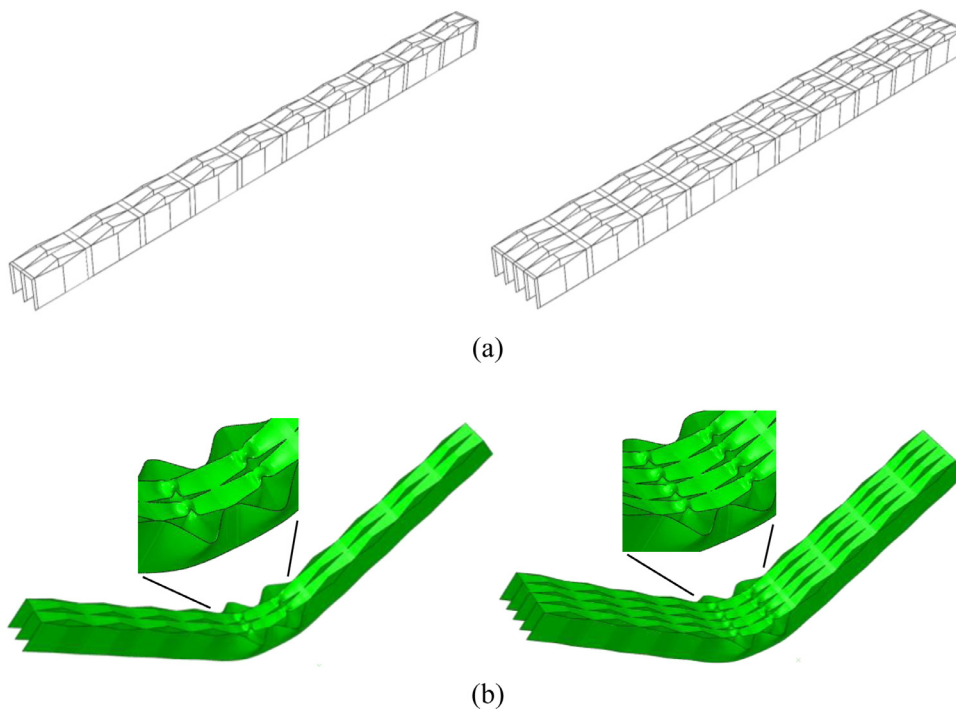
Its origami folding pattern and geometry are shown in Fig. 24. The folding pattern shown in Fig. 24(a) starts with the same form as in Fig. 2(a) on its left side and switches to a different form on the right side after going through the face-switcher in the middle section. The geometric function of this process can also be seen in Fig. 24(b), in which the structure starts with the top face facing up on the left side and ends with the bottom webs facing up on the right side. A paper folded model is presented in Fig. 24(c), and it shows that the webs are facing up on the right end. This design enables origami beams/panels to cope with different loading conditions flexibly. The geometry of a face-switcher is governed by two parameters  $a_s$  and  $a_s'$ , which are noted in Fig. 24(a). These two parameters satisfy

$$a_s = \frac{b}{2 \sin a_s} \quad (8)$$

Face-switchers enable origami beams/panels to be designed according to an anticipated moment distribution. However, face-switchers can only be utilized when  $m_b \geq 2$  due to geometrical constraints. Let us now consider adding a face-switcher with  $a_s=91.4$  mm to  $B_{1,3,2}$ . The result is named  $B_{1,3,2s}$  and is shown in Fig. 25(a). Note that the geometry at the ends of the beam is different from the geometry in the middle, and this beam can be also folded using a single sheet of material. Now, when  $B_0$ ,  $B_{1,3,2}$ , and  $B_{1,3,2s}$  are all put under the clamped boundary condition (lateral movement is allowed but rotation at the two ends is not) and loaded by a rigid cylinder as in Section 4. This boundary condition and loading cause different directions of moment in the middle and two ends of the beam, respectively. The deformations of the three beams are shown in Fig. 25. The bottom webs at the ends (connected to the boundaries) of  $B_{1,3,2}$  buckled laterally due to compression, and their stiffness were reduced significantly afterwards. In contrast, parts of  $B_{1,3,2s}$  in both the middle and ends experienced the same type of deformation, which could generate sustainable bending resistance in a large deformation. The SEAs of  $B_0$ ,  $B_{1,3,2}$ , and  $B_{1,3,2s}$  were 1514.6, 1602.3, and 2156.0 J/kg, which shows that  $B_{1,3,2s}$  achieved significantly higher energy absorption than the other two beams. These results demonstrated that the face-switcher is effective in terms of enabling origami beams or panels to cope with different loading scenarios and maximize their energy absorption capacities.

### 5.3. Origami curved beams and panels

All the beams and panels presented in the previous sections can be transformed into curved beams and curved panels by modifying their origami folding patterns, extending the applicability of these designs.

**Fig. 22.** Parametric effects on the unstable failure.**Fig. 23.** (a) Geometries of origami beams/panels with  $m_b = 2$  and  $4$ , and (b) their corresponding simulated deformations.

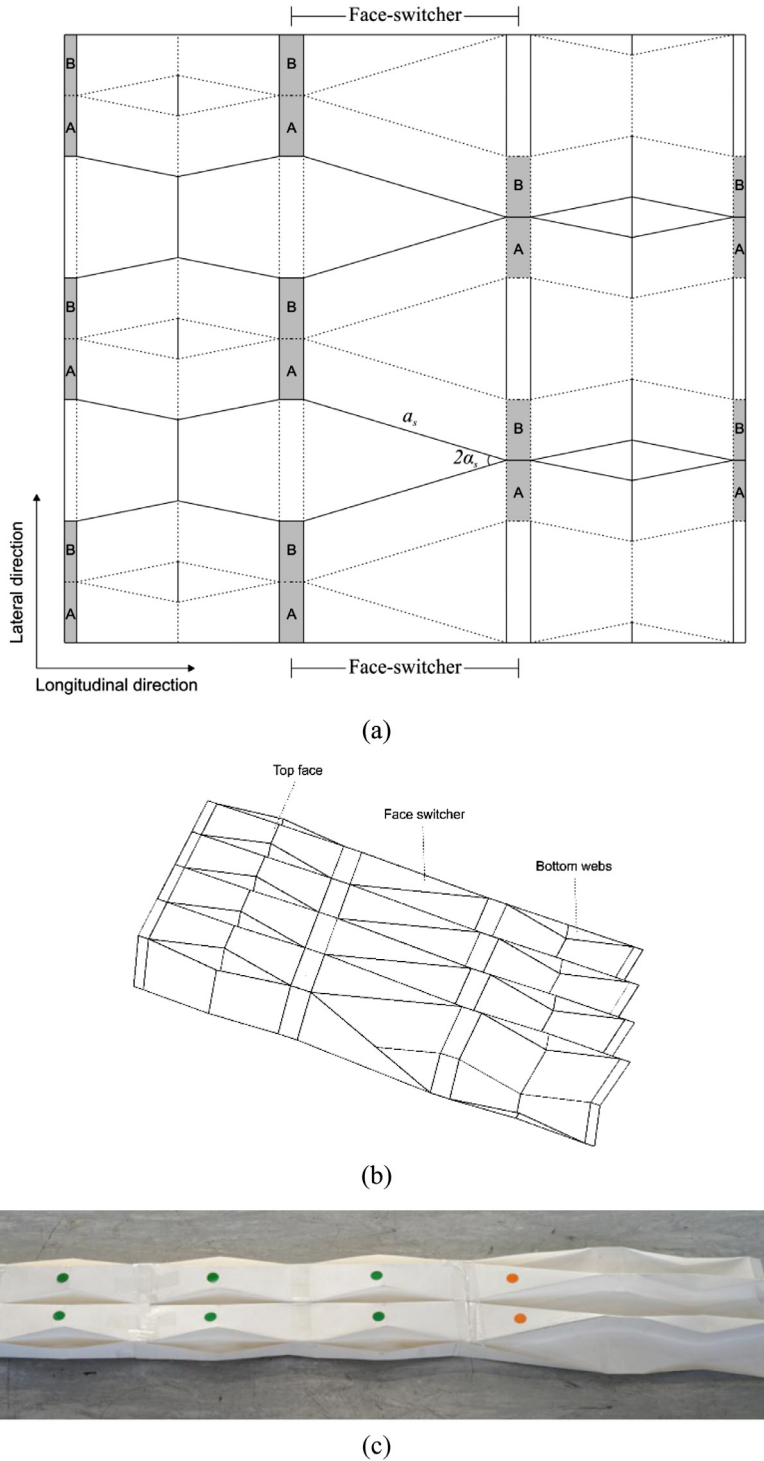


**Fig. 24.** Design of face-switcher: (a) a portion of the folding pattern; (b) geometry of the face-switcher; and (c) a paper folded model.

### 5.3.1. Geometry

There can be two directions of curvature, *curve 1* and *curve 2*, as shown in Figs. 26(a) and (b), respectively, as the result of additional folding lines being added to the origami pattern in Fig. 2(a). There are other ways of creating a curved beam from an origami beam, all of which essentially make sure that one side of beam is folded at a larger angle than the other side. The design details for origami curved beams and panels are comparable to those for beams and panels, except for the replacement of  $\alpha$  to  $\alpha_1$  and  $\alpha_2$ , as noted in Fig. 26. As in Section 5.2,

the face-switcher is also applicable in origami curved beams and panels.

### 5.3.2. Preliminary numerical simulation

A conventional curved beam  $A_0$  was designed according to Fig. 5, with a radius of 2832 mm, depth of 55 mm, and span of 983.5 mm, based on the measurements, which is shown in Fig. 27(a). Based on parameters of  $B_{1,3}$ , a numerical model of an origami curved beam  $A_1$  was made utilizing curve 1 geometry, as shown in Fig. 27(a). The

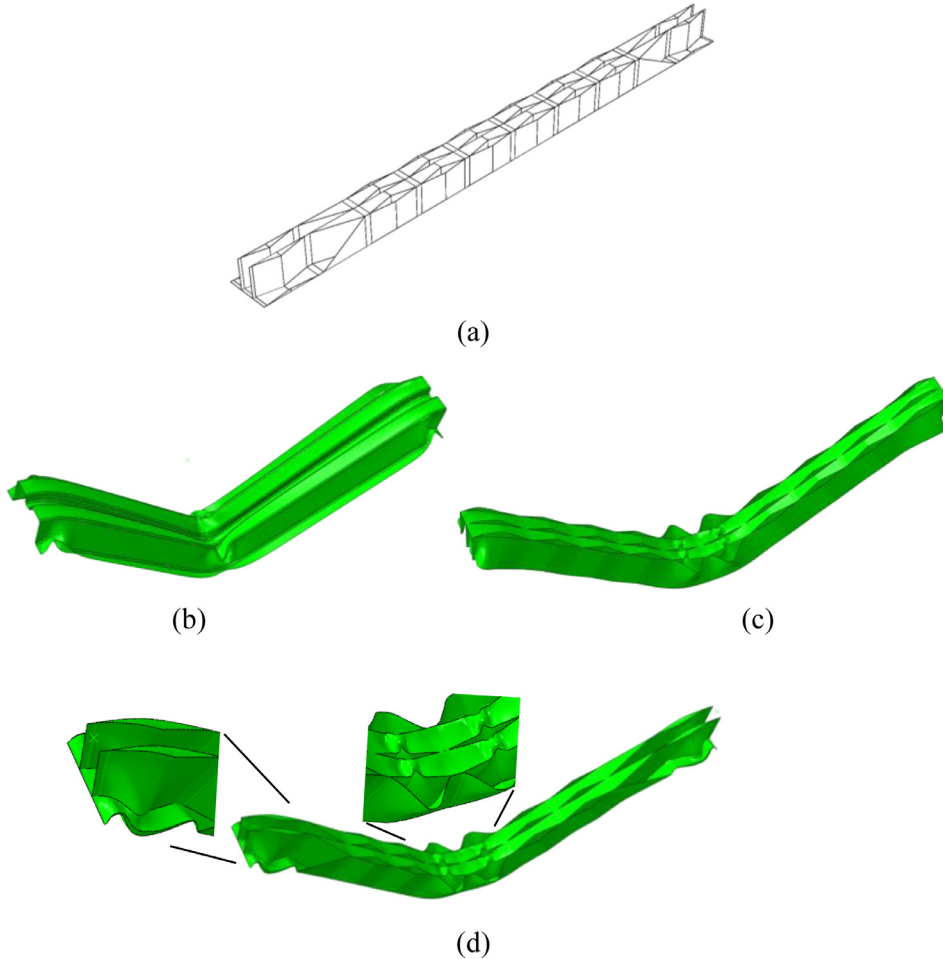


**Fig. 25.** (a) Geometry of  $B_{1,3,2s}$ , and simulated deformation of (b)  $B_0$ , (c)  $B_{1,3,2}$ , and (d)  $B_{1,3,2s}$  with a displacement of 250 mm.

values of  $\alpha_1$  and  $\alpha_2$  were  $77.7^\circ$  and  $83.7^\circ$ , respectively, and all other parameters were the same as those for beam  $B_{1,3}$ . Hence,  $A_1$  had the same radius, depth, and span as  $A_0$ . Numerical simulations of the three-point bending (as in Section 4) of the two curved beams were done, and the resulting deformations are shown in Fig. 27(b), with SEAs of 641.9 and 735.0 J/kg for  $A_0$  and  $A_1$ , respectively. The material in the middle of the origami curved beam  $A_1$  bulged upwards just like in the origami beam (Fig. 19), while  $A_0$  demonstrated a reduction in section height.

Origami curved panels with  $m_b = 2$  and 4, named  $A_2$  and  $A_3$ , respectively, were also numerically simulated, as shown in Fig. 28. They exhibited the same failure mechanism as  $A_1$ . The SEAs of  $A_1$ ,  $A_2$ , and  $A_3$  were 735.0, 869.4, and 999.3 J/kg, respectively, which indicates that higher SEAs can be achieved by adding more lateral units.

As in Section 5.2, face-switchers can be also introduced to origami curved beams and panels. A paper folded model is presented in Fig. 29(a), and it shows that the webs are facing up at the two ends of the curved beam. A numerical curved beam model with face-switchers was created and named  $A_{2s}$ , as shown in Fig. 29(b). Values of  $\alpha_1$  and  $\alpha_2$  for the curve 1 section were  $77.7^\circ$  and  $87.5^\circ$ , respectively, and  $89^\circ$  and  $80^\circ$  for the curve 2 section, respectively.  $A_{2s}$ 's other parameters were the same as  $B_{1,3,2s}$ 's, with a radius of 2820 mm and span of 989.2 mm. Numerical simulations of  $A_{2s}$  were done under the same setting used in Section 5.2. The simulated deformation is shown in Fig. 29(c) and is similar to the deformation in Fig. 25(d).

## 6. Conclusion and future work

One problem thin-walled beams suffer from when bent in large deformations is reductions in their cross-sectional heights which is known as the Brazier's effect, as shown in Fig. 10. The corresponding reaction reduction is shown in Fig. 13(a). The geometric intervention introduced in this paper is to replace straight beams with beams possessing zig-zag origami geometries, as shown in Fig. 3(b). This geometry indicates the expected positions of indentations and bulging during bending. Spot-welding is applied to stiffen the locations where indentations are expected to occur, allowing only increases in cross-sectional heights during bending, as illustrated in Fig. 4.

This paper presents a series of energy-absorbing beams built using to this idea which aim for high and sustainable bending resistance. The key solution provided in this paper is modifying the geometry to create a beam which does not suffer from section height reduction (the Brazier's effect) during large deformations. Numerical simulations and experiments have been carried out to validate the effectiveness of these new designs and demonstrated their improvements over conventional open-section beams in terms of both SEA and LU.

The basic design of origami beams was provided, and the corresponding numerical simulations with different parameters were done afterwards. These simulations indicate that 12.7–20.7% lower LUs and 23.0–40.0% higher SEAs can be achieved for these beams (with the appropriate design parameters) when compared to a typical

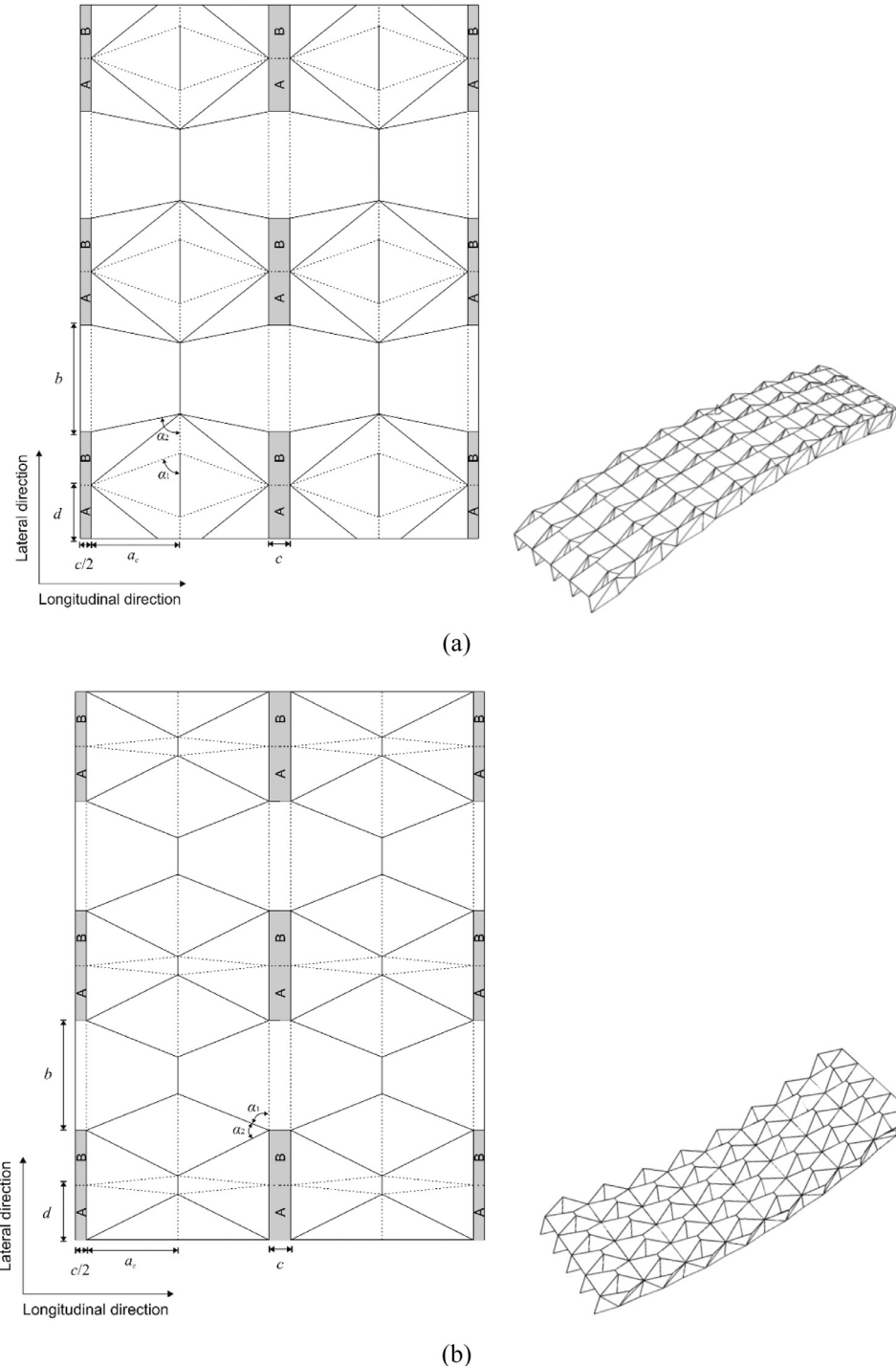


**Fig. 26.** Folding pattern and folded geometry of (a) curve 1 and (b) curve 2.

conventional open-section beam. Small-scale experiments on origami and conventional beams were compared with the numerical results. They confirmed the merits of origami beams and the accuracy of the numerical simulations used in this paper. Further geometric modifications of the basic origami beam were also presented. Origami panels can be made with a larger number of lateral units, significantly increasing their SEAs and stability. Since the top face of an origami beam/panel is designed for compression and the bottom webs for tension, the face-switcher is introduced to enable them to switch their face-sides within

the beam/panel to cope with different pre-decided loading scenarios. Further, origami curved beams and panels can be made by altering the folding patterns of origami beams and panels, resulting in performances similar to those of the origami beams based on preliminary simulations.

In terms of the research into origami beams, a number of designs and possibilities based on the same idea are presented, opening many more avenues for further research. A varieties of beams are proposed, but only the basic design of the origami beam has been examined carefully. More work can be done to analyse the other proposed structures both

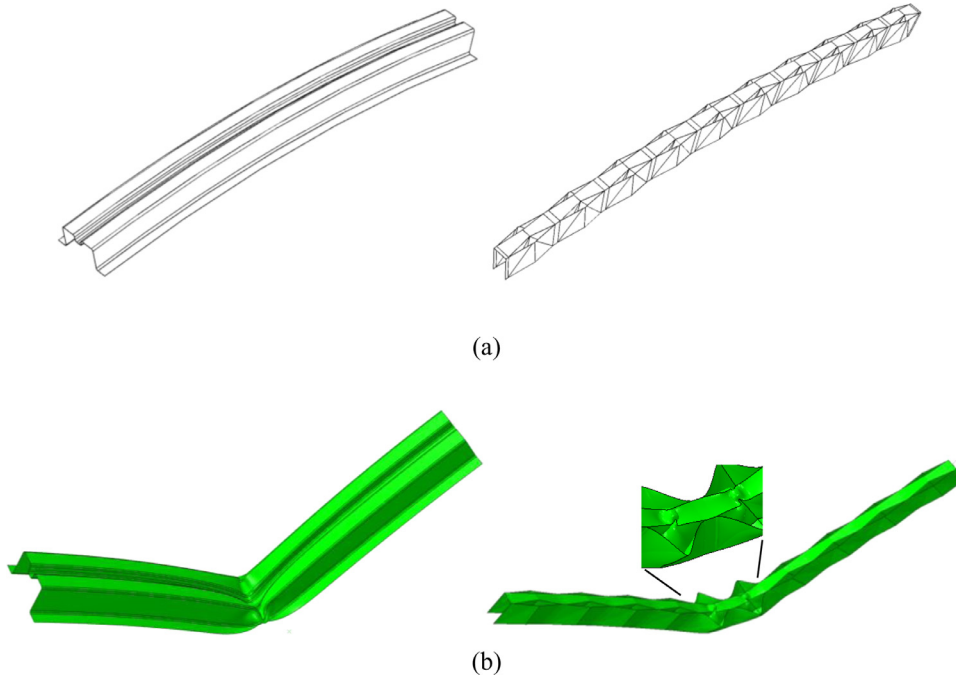


**Fig. 27.** (a) Geometries and (b) simulated deformation with displacement of 300 mm of conventional curved beam  $A_0$  and origami curved beam  $A_1$ .

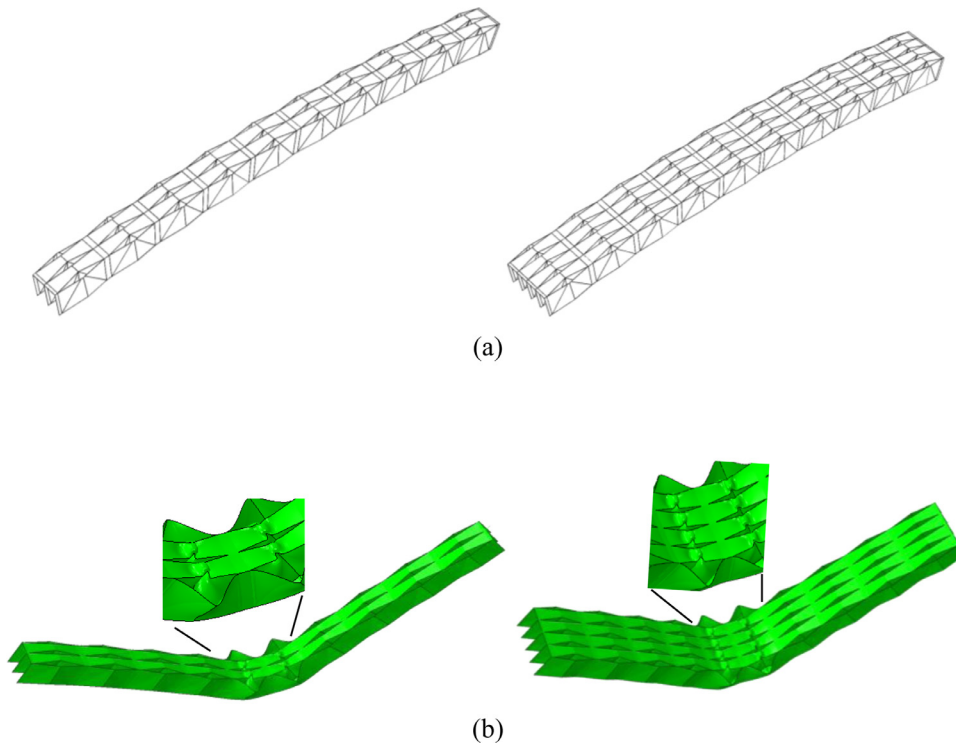


**Fig. 28.** (a) Geometries and (b) simulated deformation with displacement of 300 mm of curved origami beams/panels with  $m_b = 2$  and 4.

numerically and experimentally. More geometric modifications can be explored. For instance, the origami beam can be designed to be symmetric vertically (the top face and bottom web would then be the same). Also, theoretical models can be developed to estimate their energy absorption. Other applications of these structures can be investigated, such as being used to improve the energy absorption of slim struts in global buckling. In order to develop these designs into actual products, fur-

ther follow-up investigations are required, such as identification of specific applications, full-scale experiments, installation designs, and so on. Other concepts for improving the bending resistance in large deformations can be explored. For instance, a thin-walled bending module, which can be hardened (increasing its stiffness) during bending through self-contact, other geometric deformations, and material hardening, could be investigated.

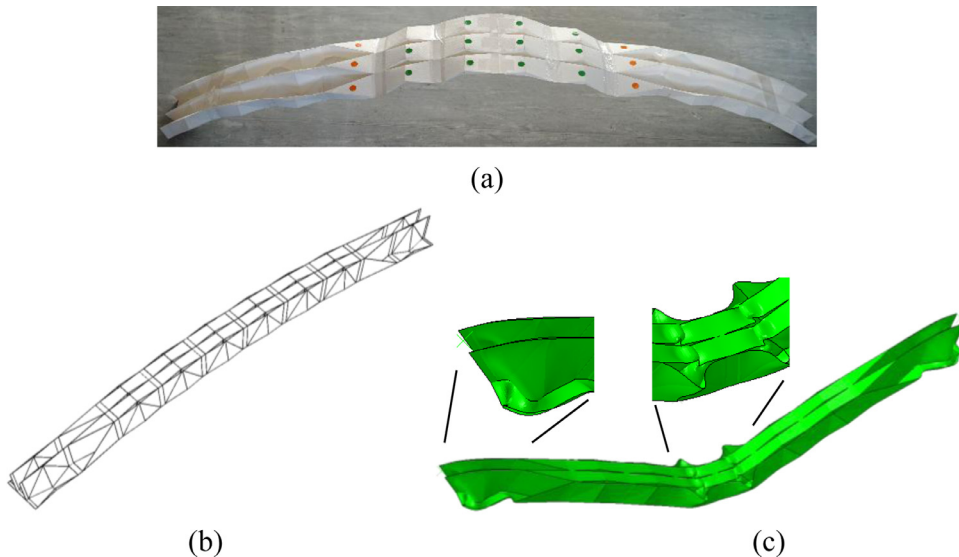


**Fig. 29.** (a) Paper folded model, (b) numerical geometry, and (c) simulated deformation with displacement of 300 mm of a curved origami beam with face-switcher.

## Acknowledgement

The authors wish to acknowledge the support of the Air Force Office of Scientific Research (FA9550-16-1-0339).

## References

- [1] Lu G, u T. Energy absorption of structures and materials. CRC Press; 2003.
- [2] Calladine CR. Theory of shell structures. Cambridge University Press; 1989.
- [3] Huang Z, Zhang X. Three-point bending collapse of thin-walled rectangular beams. *Int J Mech Sci* 2018;144:461–79.
- [4] Schwartz, R. and Ramoo, R. (1999), Energy absorbing bumper, US Patent, 6,007,123.
- [5] Ma J, You Z. Energy absorption of thin-walled beams with a pre-folded origami pattern. *Thin-Wall Struct* 2013;73:198–206.
- [6] Zou M, et al. Bionic design of the bumper beam inspired by the bending and energy absorption characteristics of bamboo. *Appl Bionics Biomech* 2018;2018:12.
- [7] Hosseinzadeh R, Shokrieh MM, Lessard LB. Parametric study of automotive composite bumper beams subjected to low-velocity impacts. *Compos Struct* 2005;68(4):419–27.
- [8] Gattas JM, You Z. The behaviour of curved-crease foldcores under low-velocity impact loads. *Int J Solids Struct* 2015;53:80–91.
- [9] Gattas JM, You Z. Quasi-static impact of indented foldcores. *Int J Impact Eng* 2014;73:15–29.
- [10] Abaqus. Abaqus documentation version 6.13. Providence, RI, USA: Dassault Systems SIMULIA Corp.; 2013.
- [11] Ma J, You Z. Energy absorption of thin-walled square tubes with a prefolded origami pattern—Part I: geometry and numerical simulation. *J Appl Mech* 2013;81(1):011003.
- [12] Li Y, You Z. Thin-walled open-section origami beams for energy absorption. In: Proceedings of the ASME 2014 international design engineering technical conferences and computers and information in engineering conference. 17–20 August, Buffalo, New York; , 2014.
- [13] Sreerama P, Rao K. Design and impact analysis on front bumper beam crash box for a sedan car using glass fiber reinforced polymer. *Int J Comput Sci Math Eng* 2016.